Supporting Information

Enhancing NO electroreduction on N/O co-coordinated single-atom catalysts via d-band center modulation

Shuigen Zhu,[1‡] Hao Yuan,[1‡] Yu Zhang,[1] Guobing Zhou,*[,1,2] Zhen Yang*[,1,2]

[1]*School of Chemical Engineering, College of Chemistry and Materials, Jiangxi Normal University, Nanchang 330022, China*

[2]*National Engineering Research Center for Carbohydrate Synthesis, Key Lab of Fluorine and Silicon for Energy Materials and Chemistry of Ministry of Education, Jiangxi Normal University, Nanchang 330022, China*

‡These authors contributed equally

S1. The calculation of constant potential

The double-reference method was employed to simulate the metal/solution interface under electrochemical conditions, enabling the evaluation of reaction energetics for ammonia (NH_3) formation on catalyst surfaces as a function of applied potential. The aqueous environment was modeled by setting the relative permittivity of the electrolyte to 80, while the cavity energy contribution was neglected. The compensating charge distribution was described using the linearized Poisson–Boltzmann model, with a Debye screening length fixed at 3.0 Å. The system's potential-dependent energy (E) is calculated as: [S1]

$$E = E_{DFT} - \Delta_n(V_{sol} + \phi q/e) \quad (1)$$

E_{DFT} refers to the energy calculated from electrochemical density functional theory. Vsol is the potential of the bulk electrolyte. Φq is the work function of the charged slab. The potential of the charged slab relative to the Standard Hydrogen Electrode (SHE) is as follows:

$$U_q(V/SHE) = -4.6V - (\phi q/e) \quad (2)$$

For each structure, the excess charge (Δn) is set from -2 to 2 e^-, in increments of 0.5 e^-, to simulate the charged surface under applied voltage. The total free energy is then fitted to a quadratic function to provide the free energy as a continuous function of potential. The points of E−Uq follow a quadratic function.[S1]

$$E(U_q) = -\frac{1}{2}C(U_q - U_0)^2 + E_0 \quad (3)$$

where U_0 is the potential of zero charge (PZC), C is the capacitance of the corresponding system, and E_0 is the fitted value of the system's energy at the PZC.

$$E_{ads}(*NO) = E(*NO) - E(slab) - E(NO) \quad (4)$$

$$E_{ads}(*HNO) = E(*HNO) - E(slab) - E(NO) - \frac{1}{2}E(H_2) \quad (5)$$

$$E_{ads}(*NOH) = E(*NOH) - E(slab) - E(NO) - \frac{1}{2}E(H_2) \quad (5)$$

$$E_{ads}(*HNOH) = E(*HNOH) - E(slab) - E(NO) - E(H_2) \quad (6)$$

$$E_{ads}(*HN_2OH) = E(*HN_2OH) - E(slab) - E(*HN_2OH) \quad (7)$$

$$E_{ads}(*NH_2) = E(*NH_2) + E(H_2O) - E(slab) - E(NO) - 2E(H_2) \quad (8)$$

$$E_{ads}(*NH_3) = E(*NH_3) - E(slab) - E(NH_3) \quad (9)$$

S2. The calculation of surface Pourbaix diagrams.

Surface Pourbaix diagrams are fundamental tools for evaluating the stability of catalyst surfaces and plausible electrochemical reactions occurring thereon under varying electrode potentials and pH conditions. In such diagrams, the horizontal axis typically denotes the pH value, while the vertical axis represents the electrode potential relative to the standard hydrogen electrode (SHE).[S2] Each region in the diagram corresponds to the thermodynamically stable form of species adsorbed on the catalyst surface under specific (potential-pH) conditions. For catalytic systems, oxygen-containing functional groups adsorbed on the catalyst surface can be broadly defined by the general formula OmHn ,

$$* - O_m H_n + (2m - n)\,(e^- + H^+) \;\leftrightarrow\; m H_2 O \tag{10}$$

where m and n represent the number of adsorbed oxygen and hydrogen atoms, respectively, and the associated change in Gibbs free energy can be calculated.

$$\Delta G(U, pH) = G * + m\, G_{H_2O} - G_{*-O_m H_n} - (2m - n)(G_{e^-} + G_{e^+}) \tag{11}$$

According to the CHE model, the Gibbs free energy of proton/electron pairs can be represented on the standard hydrogen electrode (SHE) scale as 1/2 H_2

$$(G_{e^-} + G_{e^+}) = \frac{1}{2} G_{H_2} - eU_{SHE} + k_B T(In[a_{H^+}]) \tag{12}$$

where k_B and T refer to the Boltzmann constant and the temperature, respectively, and the value of T was taken as 298.15 K. Based on the aforementioned equations, it is possible to establish a relationship between potential and pH for a broad spectrum of oxygen-containing adsorbates on catalysts surfaces, corresponding to standard conditions where the change in Gibbs free energy ΔG (U, pH) equals zero.

S3. Binding energies of metal atoms in N/O co-doped graphene

Table S1. Calculated binding energies of different metal centers on 1N,3O co-doped graphene (gra-N1O3). E_M: energy of an isolated metal atom; $E_{gra\text{-}N1O3}$: energy of gra-N1O3; $E_{M\text{-}N1O3}$: energy of the gra-N1O3 anchored with metal atom; $E_{binding}$: binding energy between the metal atom and the gra-N1O3 substrate.

Metal	E_M (eV)	$E_{gra\text{-}N1O3}$ (eV)	$E_{M\text{-}N1O3}$ (eV)	$E_{binding}$ (eV)
Sc	-2.08	-857.12	-863.13	-3.93
Ti	-2.42	-857.12	-863.56	-4.02
V	-3.60	-857.12	-864.03	-3.32
Cr	-5.44	-857.12	-864.57	-2.02
Mn	-5.15	-857.12	-863.11	-0.84
Fe	-2.99	-857.12	-862.70	-2.60
Co	-1.49	-857.12	-861.80	-3.20
Ni	-0.35	-857.12	-860.68	-3.21
Cu	-0.23	-857.12	-858.96	-1.62
Zn	-0.01	-857.12	-857.49	-0.37

Table S2. Calculated binding energies of different metal centers on 2N,2O co-doped graphene (gra-N2O2α). E_M: energy of an isolated metal atom; $E_{gra\text{-}N2O2\alpha}$: energy of gra-N2O2α; $E_{M\text{-}N2O2\alpha}$: energy of the gra-N_2O_2α anchored with metal atom; $E_{binding}$: binding energy between the metal atom and the gra-N2O2α substrate.

Metal	E_M (eV)	$E_{gra\text{-}N2O2\alpha}$(eV)	$E_{M\text{-}N2O2\alpha}$(eV)	$E_{binding}$ (eV)
Sc	-2.08	-859.32	-866.45	-5.04
Ti	-2.42	-859.32	-866.95	-5.20
V	-3.60	-859.32	-867.42	-4.50
Cr	-5.44	-859.32	-866.45	-1.69
Mn	-5.15	-859.32	-867.24	-2.78
Fe	-2.99	-859.32	-866.49	-4.18
Co	-1.49	-859.32	-865.53	-4.72
Ni	-0.35	-859.32	-861.97	-4.30
Cu	-0.23	-859.32	-859.49	-2.41
Zn	-0.01	-859.32	-866.45	-0.16

Table S3. Calculated binding energies of different metal centers on 2N,2O co-doped graphene (gra-N2O2β). E_M: energy of an isolated metal atom; $E_{gra\text{-}N2O2\beta}$: energy of gra-N2O2β; $E_{M\text{-}N2O2\beta}$: energy of the gra-N2O2β anchored with metal atom; $E_{binding}$: binding energy between the metal atom and the gra-N2O2β substrate.

Metal	E_M (eV)	$E_{gra\text{-}N2O2\beta}$(eV)	$E_{M\text{-}N2O2\beta}$(eV)	$E_{binding}$ (eV)
Sc	-2.08	-858.83	-866.46	-5.55
Ti	-2.42	-858.83	-867.04	-5.79
V	-3.60	-858.83	-867.74	-5.31
Cr	-5.44	-858.83	-868.41	-4.14
Mn	-5.15	-858.83	-866.78	-2.81
Fe	-2.99	-858.83	-866.68	-4.87
Co	-1.49	-858.83	-865.64	-5.32
Ni	-0.35	-858.83	-864.07	-4.89
Cu	-0.23	-858.83	-862.07	-3.02
Zn	-0.01	-858.83	-859.77	-0.93

Table S4. Calculated binding energies of different metal centers on 2N,2O co-doped graphene (gra-N2O2γ). E_M: energy of an isolated metal atom; $E_{gra\text{-}N2O2\gamma}$: energy of gra-N2O2γ; $E_{M\text{-}N2O2\gamma}$: energy of the gra-N2O2γ anchored with metal atom; $E_{binding}$: binding energy between the metal atom and the gra-N2O2γ substrate.

Metal	E_M (eV)	$E_{gra\text{-}N2O2\gamma}$(eV)	$E_{M\text{-}N2O2\gamma}$(eV)	$E_{binding}$ (eV)
Sc	-2.08	-859.26	-866.69	-5.35
Ti	-2.42	-859.26	-867.04	-5.36
V	-3.60	-859.26	-867.74	-4.88
Cr	-5.44	-859.26	-868.41	-3.71
Mn	-5.15	-859.26	-866.78	-2.37
Fe	-2.99	-859.26	-866.68	-4.43
Co	-1.49	-859.26	-865.64	-4.89
Ni	-0.35	-859.26	-864.07	-4.45
Cu	-0.23	-859.26	-861.92	-2.43
Zn	-0.01	-859.26	-859.77	-0.50

Table S5. Calculated binding energies of different metal centers on 3N,1O co-doped graphene (gra-N3O1). E_M: energy of an isolated metal atom; $E_{gra\text{-}N3O1}$: energy of gra-N3O1; $E_{M\text{-}N3O1}$: energy of the gra-N3O1 anchored with metal atom; $E_{binding}$: binding energy between the metal atom and the gra-N3O1 substrate.

Metal	E_M (eV)	$E_{gra\text{-}N3O1}$ (eV)	$E_{M\text{-}N3O1}$ (eV)	$E_{binding}$ (eV)
Sc	-2.08	-860.82	-869.99	-7.08
Ti	-2.42	-860.82	-870.48	-7.24
V	-3.60	-860.82	-871.03	-6.61
Cr	-5.44	-860.82	-871.75	-5.49
Mn	-5.15	-860.82	-871.04	-5.08
Fe	-2.99	-860.82	-870.12	-6.31
Co	-1.49	-860.82	-869.22	-6.90
Ni	-0.35	-860.82	-867.58	-6.41
Cu	-0.23	-860.82	-865.10	-4.05
Zn	-0.01	-860.82	-863.16	-2.33

Table S6. Calculated binding energies of different metal centers on 4N doped graphene (gra-N4). E_M: energy of an isolated metal atom; $E_{gra\text{-}N4}$: energy of gra-N4; $E_{M\text{-}N4}$: energy of the gra-N4 anchored with metal atom; $E_{binding}$: binding energy between the metal atom and the gra-N4 substrate.

Metal	E_M (eV)	$E_{gra\text{-}N4}$ (eV)	$E_{M\text{-}N4}$ (eV)	$E_{binding}$ (eV)
Sc	-2.08	-862.72	-873.40	-8.60
Ti	-2.42	-862.72	-873.75	-8.61
V	-3.60	-862.72	-874.24	-7.93
Cr	-5.44	-862.72	-875.06	-6.90
Mn	-5.15	-862.72	-874.65	-6.79
Fe	-2.99	-862.72	-873.52	-7.82
Co	-1.49	-862.72	-872.47	-8.26
Ni	-0.35	-862.72	-873.40	-10.33
Cu	-0.23	-862.72	-868.33	-5.39
Zn	-0.01	-862.72	-866.30	-3.58

S4. Adsorption energies of NO molecule on M-N_xO_{4-x} ($1 \leq x \leq 4$) SACs

Table S7.Adsorption energies of NO molecule (ΔE_{*NO}) on M-N_1O_3 with different adsorption patterns. Note: the red color indicates the most stable adsorption pattern.

ΔE_{*NO} (eV)				
		N-end	**O-end**	**Side-on**
M-N_1O_3	**Sc**	-3.18	-1.58	/
	Ti	-3.40	-2.13	-4.01
	V	-3.53	-1.67	/
	Cr	-2.79	-1.24	/
	Mn	-3.48	-1.49	/
	Fe	-3.30	-1.81	/
	Co	-2.76	-1.10	/
	Ni	-2.53	-1.92	/
	Cu	-1.86	-1.35	/
	Zn	-0.75	0.68	/

Table S8. Adsorption energies of NO molecule (ΔE_{*NO}) on M-$N_2O_2\alpha$ with different adsorption patterns. Note: the red color indicates the most stable adsorption pattern.

ΔE_{*NO} (eV)				
		N-end	**O-end**	**Side-on**
M-$N_2O_2\alpha$	**Sc**	-2.82	-2.33	/
	Ti	-3.22	-2.01	-3.56
	V	-3.32	-1.68	/
	Cr	-2.72	-0.98	/
	Mn	-2.88	-1.08	/
	Fe	-2.47	-0.52	/
	Co	-2.19	-0.46	/
	Ni	-2.24	-0.36	/
	Cu	-1.72	-0.88	/
	Zn	-1.79	-0.51	/

Table S9. Adsorption energies of NO molecule (ΔE_{*NO}) on M-$N_2O_2\beta$ with different adsorption patterns. Note: the red color indicates the most stable adsorption pattern.

ΔE_{*NO} (eV)				
		N-end	**O-end**	**Side-on**
M-$N_2O_2\beta$	**Sc**	-2.98	-2.52	/
	Ti	-3.24	-2.18	-3.77
	V	-3.18	-1.52	-3.32
	Cr	-2.63	-0.79	/
	Mn	-3.01	-0.75	/
	Fe	-2.53	-1.53	/
	Co	-2.18	-0.47	/
	Ni	-1.76	-0.16	/
	Cu	-1.21	-0.80	/
	Zn	-1.32	-0.88	/

Table S10. Adsorption energies of NO molecule (ΔE_{*NO}) on M-$N_2O_2\gamma$ with different adsorption patterns. Note: the red color indicates the most stable adsorption pattern.

ΔE_{*NO} (eV)				
		N-end	**O-end**	**Side-on**
M-$N_2O_2\gamma$	**Sc**	-2.82	-2.38	/
	Ti	-3.25	-2.22	-3.53
	V	-3.16	-1.58	-3.19
	Cr	-2.69	-0.86	/
	Mn	-3.12	-1.99	/
	Fe	-2.33	-0.57	/
	Co	-1.89	-0.57	/
	Ni	-2.26	-0.15	/
	Cu	-1.78	-0.84	/
	Zn	-1.42	-0.91	/

Table S11. Adsorption energies of NO molecule (ΔE_{*NO}) on M-N_3O_1 with different adsorption patterns. Note: the red color indicates the most stable adsorption pattern.

ΔE_{*NO} (eV)				
		N-end	**O-end**	**Side-on**
M-N_3O_1	**Sc**	-2.68	-2.24	/
	Ti	-3.10	-2.07	-3.30
	V	-3.22	-1.64	/
	Cr	-2.77	-0.93	/
	Mn	-2.67	-0.72	/
	Fe	-2.32	-0.76	/
	Co	-1.63	-0.56	/
	Ni	-1.32	0.04	/
	Cu	-1.18	-0.32	/
	Zn	-1.05	-0.11	/

Table S12. Adsorption energies of NO molecule (ΔE_{*NO}) on M-N_4 with different adsorption patterns. Note: the red color indicates the most stable adsorption pattern.

ΔE_{*NO} (eV)				
		N-end	**O-end**	**Side-on**
M-N_4	**Sc**	-2.36	-1.90	/
	Ti	-3.12	-2.22	-3.25
	V	-3.18	-1.85	/
	Cr	-2.94	-1.11	/
	Mn	-2.56	-0.77	/
	Fe	-2.23	-0.73	/
	Co	-1.77	-0.58	/
	Ni	-0.52	-0.22	/
	Cu	-0.44	-0.15	/
	Zn	-0.37	-0.10	/

S5. Gibbs free energies of intermediates on M-N_xO_{4-x} SACs.

Table S13. Gibbs free energies of *NO, *H, *NOH, and *HNO intermediates on the M-N_1O_3 catalysts surface.

	Metal	ΔG_{*NO} (eV)	ΔG_{*H} (eV)	ΔG_{*NOH} (eV)	ΔG_{*HNO} (eV)
M-N_1O_3	Sc	-2.63	-0.81	0.37	-0.96
	Ti	-3.48	-0.56	0.68	-0.04
	V	-2.97	-0.32	0.84	0.67
	Cr	-2.24	0.99	1.19	0.15
	Mn	-2.93	-0.12	1.13	0.87
	Fe	-2.69	0.06	1.79	1.36
	Co	-2.20	0.47	1.53	0.96
	Ni	-1.91	0.62	1.37	0.74
	Cu	-1.41	-0.31	1.15	0.03
	Zn	-0.26	-0.26	0.85	-0.33

Table S14. Gibbs free energies of *NO, *H, *NOH, and *HNO intermediates on the M-N_2O_2α catalysts surface, respectively.

	Metal	**ΔG_{*NO} (eV)**	**ΔG_{*H} (eV)**	**ΔG_{*NOH} (eV)**	**ΔG_{*HNO} (eV)**
M-N_2O_2α	Sc	-2.33	-0.70	0.54	-0.86
	Ti	-2.96	-0.45	0.35	-0.65
	V	-2.69	-0.28	0.16	0.54
	Cr	-2.09	0.88	0.96	0.79
	Mn	-2.31	0.40	0.96	0.86
	Fe	-1.92	0.14	1.28	0.95
	Co	-1.62	0.71	1.63	1.30
	Ni	-1.61	0.82	1.44	0.68
	Cu	-1.19	0.21	1.15	0.14
	Zn	-1.33	-1.14	0.68	0.06

Table S15. Gibbs free energies of *NO, *H, *NOH, and *HNO intermediates on the M-N_2O_2β catalysts surface, respectively.

	Metal	**ΔG_{*NO} (eV)**	**ΔG_{*H} (eV)**	**ΔG_{*NOH} (eV)**	**ΔG_{*HNO} (eV)**
M-N_2O_2β	Sc	-2.51	-0.83	0.68	-0.82
	Ti	-3.21	-0.53	0.45	-0.27
	V	-2.78	-0.16	0.43	0.51
	Cr	-2.04	0.22	1.08	0.73
	Mn	-2.46	0.41	1.49	0.93
	Fe	-1.99	0.14	1.51	1.08
	Co	-1.57	0.66	1.75	1.47
	Ni	-1.16	1.00	1.59	0.86
	Cu	-0.67	0.60	1.27	0.09
	Zn	-0.87	-0.54	0.76	-0.03

Table S16. Gibbs free energies of *NO, *H, *NOH, and *HNO intermediates on the M-$N_2O_2\gamma$ catalysts surface, respectively.

	Metal	**ΔG_{*NO} (eV)**	**ΔG_{*H} (eV)**	**ΔG_{*NOH} (eV)**	**ΔG_{*HNO} (eV)**
M-$N_2O_2\gamma$	Sc	-2.33	-0.76	0.69	-0.72
	Ti	-2.98	-0.59	0.17	-0.58
	V	-2.60	-0.25	0.15	0.59
	Cr	-2.07	0.16	0.94	0.80
	Mn	-2.47	-0.17	0.70	0.59
	Fe	-1.74	0.24	1.26	0.83
	Co	-1.26	0.49	1.05	0.82
	Ni	-1.62	0.96	1.46	0.97
	Cu	-1.20	0.38	1.12	0.15
	Zn	-0.87	-0.80	0.61	-0.37

Table S17. Gibbs free energies of *NO, *H, *NOH, and *HNO intermediates on the M-N_3O_1 catalysts surface, respectively.

	Metal	**ΔG_{*NO} (eV)**	**ΔG_{*H} (eV)**	**ΔG_{*NOH} (eV)**	**ΔG_{*HNO} (eV)**
M-N_3O_1	Sc	-2.23	-0.52	0.95	-0.46
	Ti	-2.75	-0.54	0.08	-0.86
	V	-2.65	-0.18	0.65	0.65
	Cr	-2.07	0.14	1.05	0.86
	Mn	-2.09	0.25	1.06	0.89
	Fe	-1.77	0.13	1.07	0.62
	Co	-1.06	0.46	1.39	0.65
	Ni	-0.75	1.18	1.51	0.84
	Cu	-0.64	0.95	1.41	0.16
	Zn	-0.59	-0.05	0.99	-0.14

Table S18. Gibbs free energies of *NO, *H, *NOH, and *HNO intermediates on the M-N_4 catalysts surface, **respectively.**

	Metal	**ΔG_{*NO} (eV)**	**ΔG_{*H} (eV)**	**ΔG_{*NOH} (eV)**	**ΔG_{*HNO} (eV)**
M-N_4	Sc	-1.88	-0.21	1.20	-0.57
	Ti	-2.74	-0.62	0.21	-0.73
	V	-2.62	-0.26	0.21	-0.13
	Cr	-2.27	0.14	1.29	1.01
	Mn	-1.96	0.34	1.29	0.94
	Fe	-1.70	0.42	0.99	0.43
	Co	-1.22	0.05	1.24	0.53
	Ni	0.01	1.60	1.32	0.30
	Cu	0.03	1.62	1.21	0.22
	Zn	0.12	0.77	0.71	-0.17

S6. Limiting potentials of NORR and HER on M-N_xO_{4-x} SACs

Table S19. Limiting potentials of NORR and HER on M-N_xO_{4-x} SACs

	$U_{L(NORR)}$ (V)	$U_{L(HER)}$ (V)
Sc-N_4	-0.34	-0.21
V-$N_2O_2\alpha$	-0.47	-0.31
V-$N_2O_2\beta$	-0.49	-0.38
V-$N_2O_2\gamma$	-0.46	-0.25
V-N_4	-0.34	-0.26
Cr-N_1O_3	-0.67	-0.16
Fe-N_4	-0.43	-0.42
Cu-N_1O_3	-0.07	-0.32
Cu-$N_2O_2\alpha$	-0.13	-0.21
Cu-$N_2O_2\beta$	-0.09	-0.69
Cu-$N_2O_2\gamma$	-0.15	-0.38
Cu-N_3O_1	-0.17	-0.95
Zn- N_1O_3	-0.62	-0.23
Zn-$N_2O_2\alpha$	-0.30	-1.14
Zn-$N_2O_2\beta$	-0.08	-0.55
Zn-$N_2O_2\gamma$	-0.42	-0.80
Zn- N_3O_1	-0.07	-0.04

S7. Fitted parameters of the quadratic equation

Table S20. Fitted parameters of the quadratic equation for Cu-N_2O_2β system

Reaction Intermediates	C (e/V)	U_0 (V/SHE)	E_0 (eV)
*	1.72	−0.87	−862.40
*N	1.84	−0.59	−867.53
*NO	1.89	−0.77	−875.91
*NOH	1.85	−0.74	−878.64
*HNO	1.82	−0.72	−879.64
*HNOH	1.76	−0.88	−883.52
*H_2NOH	1.77	−0.95	−888.09
*H_2NO	1.63	−0.76	−883.64
*NH	1.78	−0.55	−872.64
*NH_2	1.69	−0.59	−878.22
*NH_3	1.78	−0.99	−883.12

S8. Formation energy and dissolution potential of transition metal atoms in M-N_xO_{4-x} SACs.

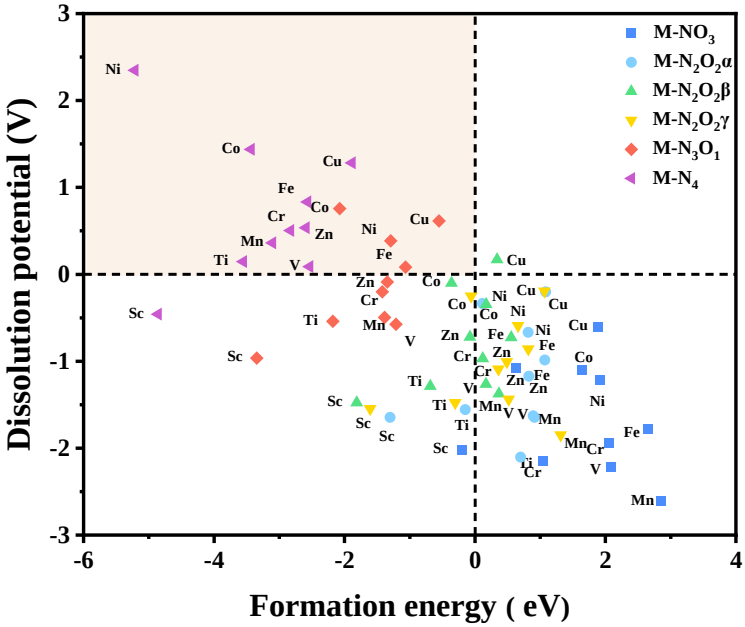

Fig. S1 Formation energy and dissolution potential of transition metal atoms in M-N_xO_{4-x} SACs.

S9. Schematic illustrations of NORR pathway

The O-end adsorption mode of NO was also examined during the initial screening; however, it was consistently found to be significantly less favourable than the N-end and side-on modes in terms of the adsorption energies in **Fig. 2** of the main text. Therefore, the O-end pathway was not considered further in the reaction-coordinate analysis.

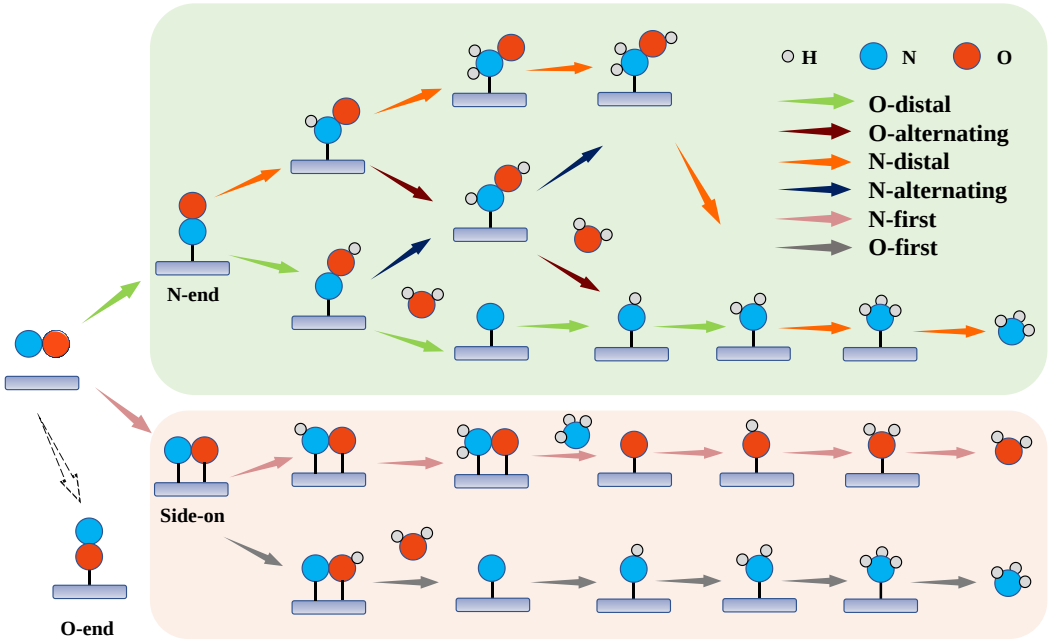

Fig. S2 Schematic illustrations of possible pathways for NORR process.

S10. Discussion on the NO adsorption configuration

In the present work, all adsorption configurations were fully relaxed before their adsorption energies were evaluated. The missing points in **Fig. 2b** of the main text do not reflect omitted data, but correspond to adsorption structures that were not retained as stable local minima after structural optimization. Side-on adsorption is often encountered in some catalytic systems; however, its stability is not universal and depends sensitively on whether the active site can simultaneously provide sufficiently strong and balanced interactions with both the N and O atoms of NO. To clarify this point, we analyzed the PDOS and ICOHP of representative Ti-N_2O_2b, V-N_2O_2b, and Cu-N_2O_2b systems, in which NO adopts a side-on configuration in the former two systems but an N-end configuration in the latter one. As shown in **Figs. S3a** and **S3b**, Ti-N_2O_2b and V-N_2O_2b exhibit clear orbital hybridization between the metal 3d states and both N 2p and O 2p states in the relevant energy region. Consistently, the corresponding ICOHP values in **Fig. S4d** indicate that both M–N and M–O interactions are simultaneously strong in these two systems (Ti: M–N = −6.04 eV, M–O = −4.60 eV; V: M–N = −6.31 eV, M–O = −4.43 eV), allowing NO to be stably anchored in a side-on manner. By contrast, for Cu-N_2O_2b, although some Cu 3d–O 2p hybridization can still be observed (see **Fig. S3c**), the corresponding Cu–O interaction is much weaker (−0.24 eV), whereas the adsorption is primarily dominated by the Cu–N interaction (−3.13 eV), as further supported by the pronounced hybridization between the metal 3d states and N 2p states in **Fig. S3c**. This imbalance between the M–N and M–O interactions makes the side-on adsorption configuration unfavourable and leads to relaxation into the N-end mode. These results indicate that the side-on adsorption mode can only be stabilized when the metal center is able to interact favorably with both the N and O atoms of the NO molecule in a sufficiently balanced manner; otherwise, the initially constructed side-on configuration would relax to an N-end structure after optimization.

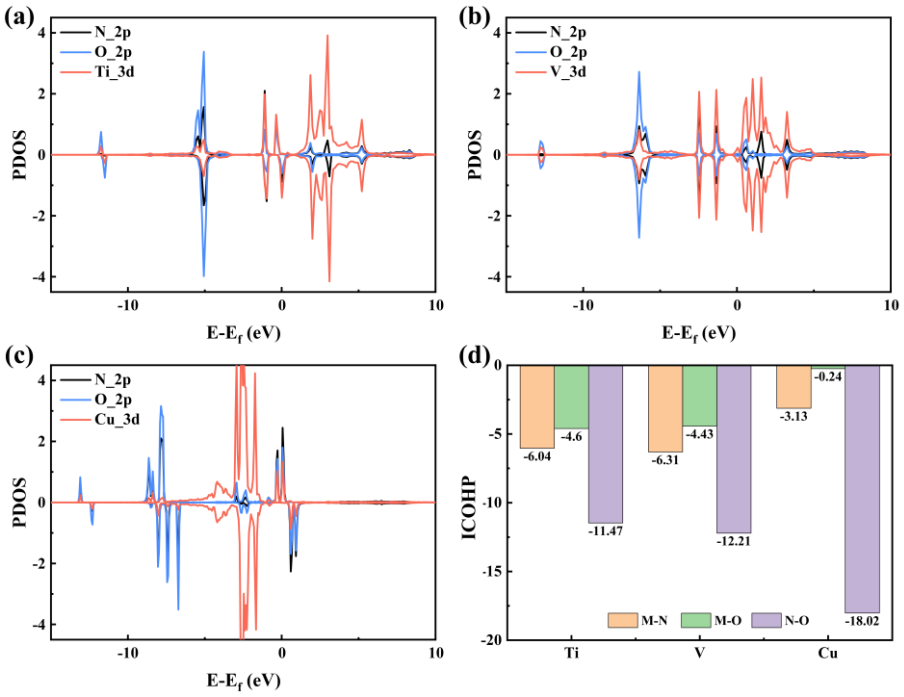

Fig. S3 Projected Density of States (PDOS) plots for (a) Ti-$N_2O_2\beta$, (b) V-$N_2O_2\beta$, and (c) Cu-$N_2O_2\beta$. (d) Integrated Crystal Orbital Hamilton Population (ICOHP) values for M-N, M-O, and N-O bonds across the three SACs.

S11. Gibbs free energies of key intermediates on M–N_xO_y SACs

To better understand the anomalous behavior of Sc in **Fig. 2c** of the main text and **Figs. S4** and **S5**, we compared the bonding characteristics of Sc- and Ti-based systems, since Ti is the adjacent 3d metal and basically follows the general trend. Our additional ICOHP analysis shows that, in the Sc systems, *NO, *HNO, and *NOH are all mainly bonded to the metal center through the N atom. We therefore used the M–N ICOHP values to qualitatively compare the interaction strength between the metal center and these adsorbates in Sc- and Ti-based SACs. The results in **Fig. S6** show that the Ti–N ICOHP values are consistently more negative than the corresponding Sc–N ICOHP values for *NO, *HNO, and *NOH, indicating stronger Ti–N bonding interactions and thus stronger Ti–adsorbate interactions than in the Sc systems. This bonding picture is qualitatively consistent with the calculated adsorption energetics: Ti generally exhibits more negative adsorption free energies for *NO, *HNO, and *NOH than Sc, implying stronger stabilization of these intermediates. Therefore, we consider that the anomalous behavior of Sc can be rationalized, at least qualitatively, by the weaker Sc–N interaction with NO-derived intermediates relative to Ti.

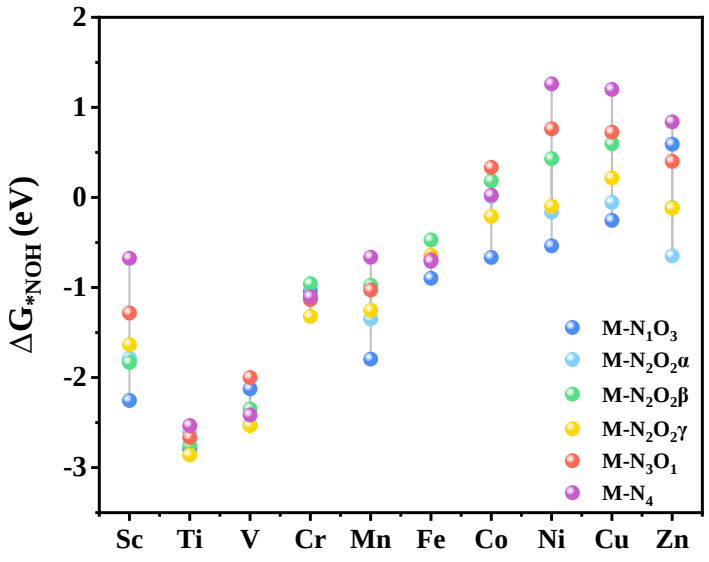

Fig. S4 Gibbs free energy of *NOH (ΔG_{*NOH}) on five studied M–N_xO_y SACs with metal atoms from Sc to Zn.

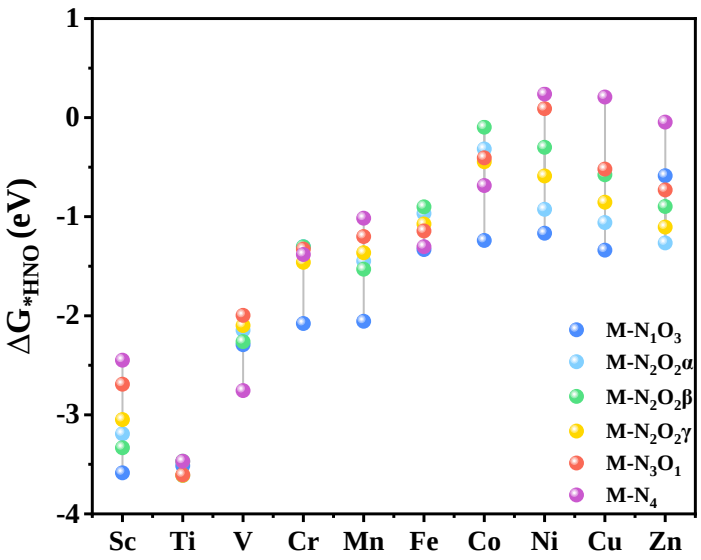

Fig. S5 Gibbs free energy of *HNO (ΔG_{*HNO}) on five studied M–N_xO_y SACs with metal atoms from Sc to Zn.

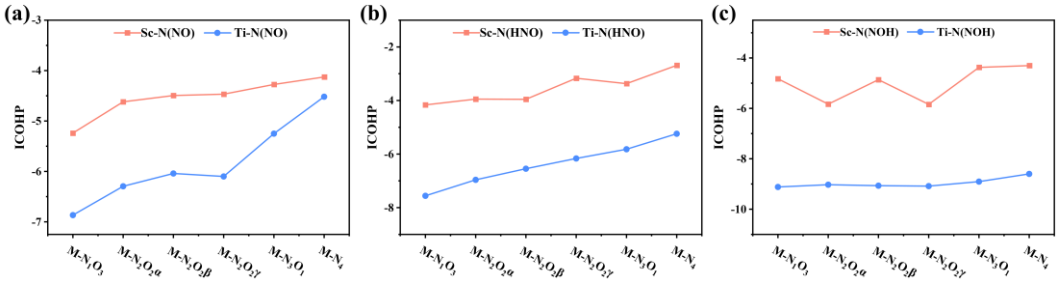

Fig. S6 M–N ICOHP values of Sc- and Ti-based SACs with different coordination environments for adsorbed (a) *NO, (b) *HNO, and (c) *NOH intermediates.

S12. Linear correlations of ΔG_{*NO} with ΔG_{*HNO} and ΔG_{*NOH}

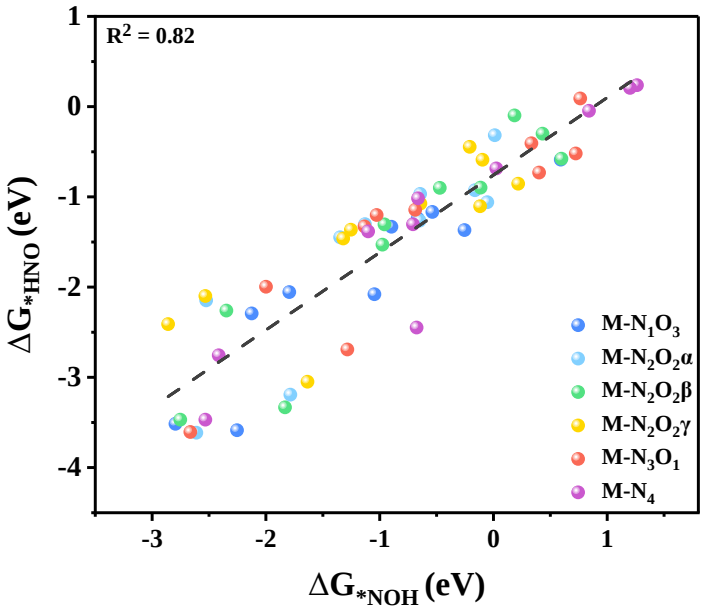

Fig. S7 Linear correlation between ΔG_{*HNO} and ΔG_{*NOH} across all M–N_xO_y SACs.

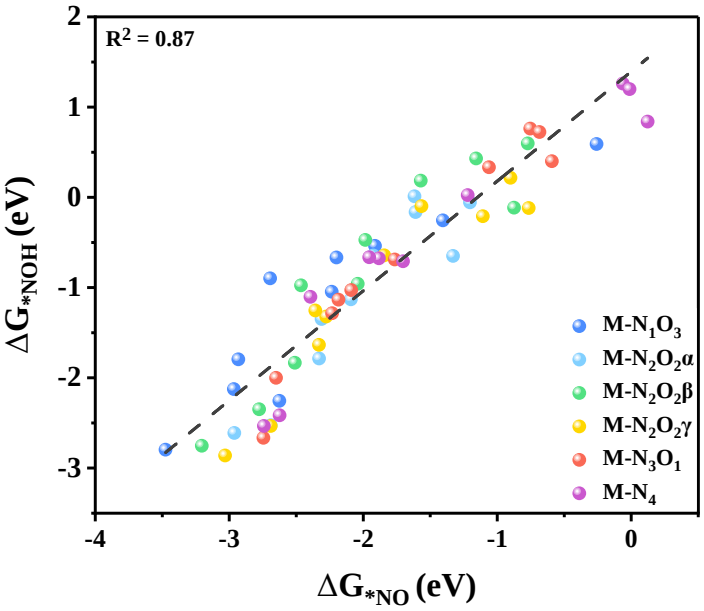

Fig. S8 Linear correlation between ΔG_{*NO} and ΔG_{*NOH} across all M–N_xO_y SACs.

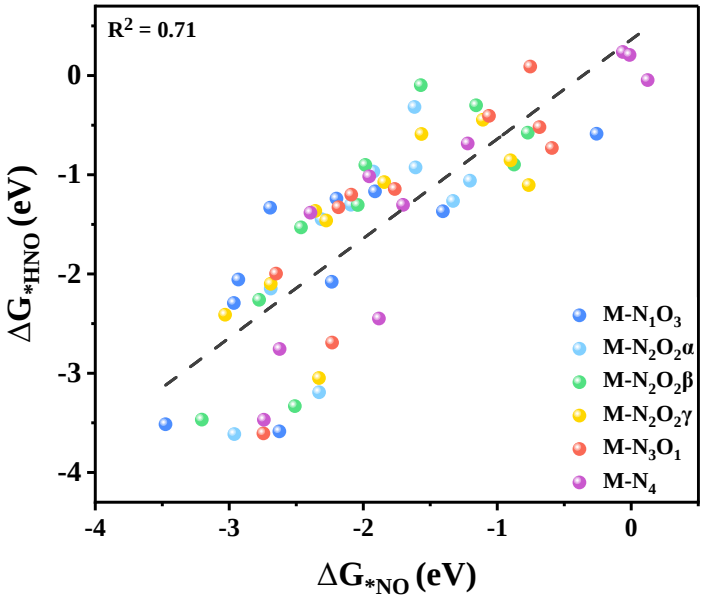

Fig. S9 Linear correlation between ΔG_{*NO} and ΔG_{*HNO} across all M–N_xO_y SACs.

S13. Free energy diagrams of NORR on screened M-N_xO_{4-x} SACs

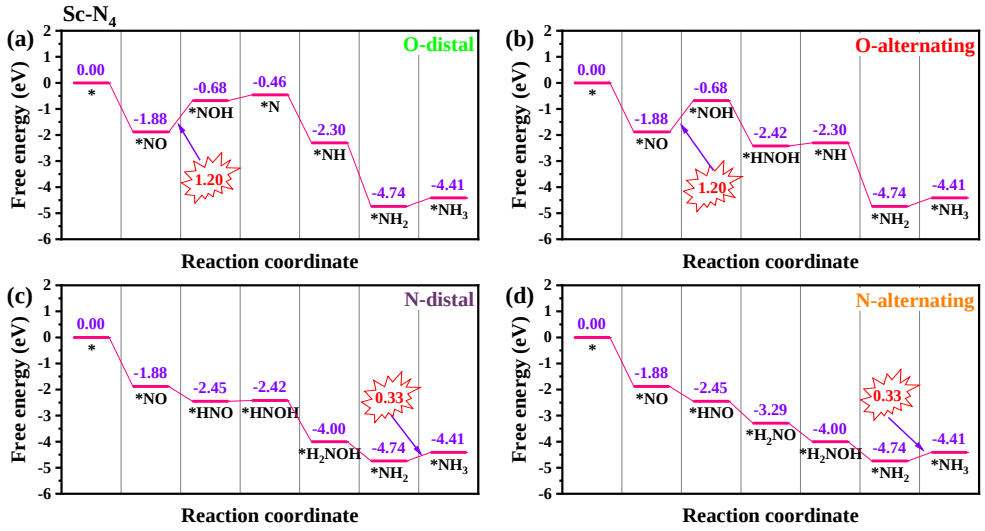

Fig. S10 Free energy diagrams of NORR on Sc-N_4 SAC.

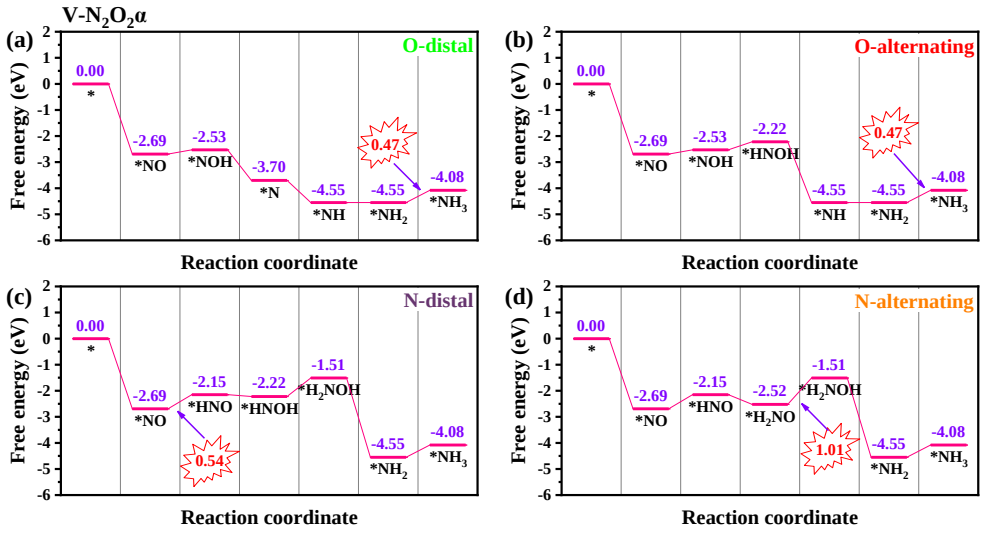

Fig. S11 Free energy diagrams of NORR on V-N_2O_2α SAC.

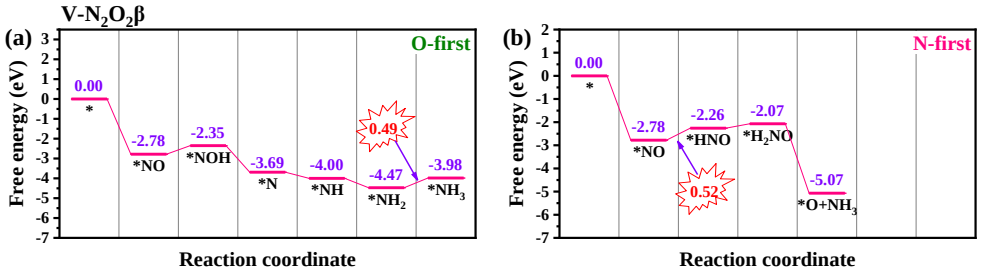

Fig. S12 Free energy diagrams of NORR on V-N_2O_2β SAC.

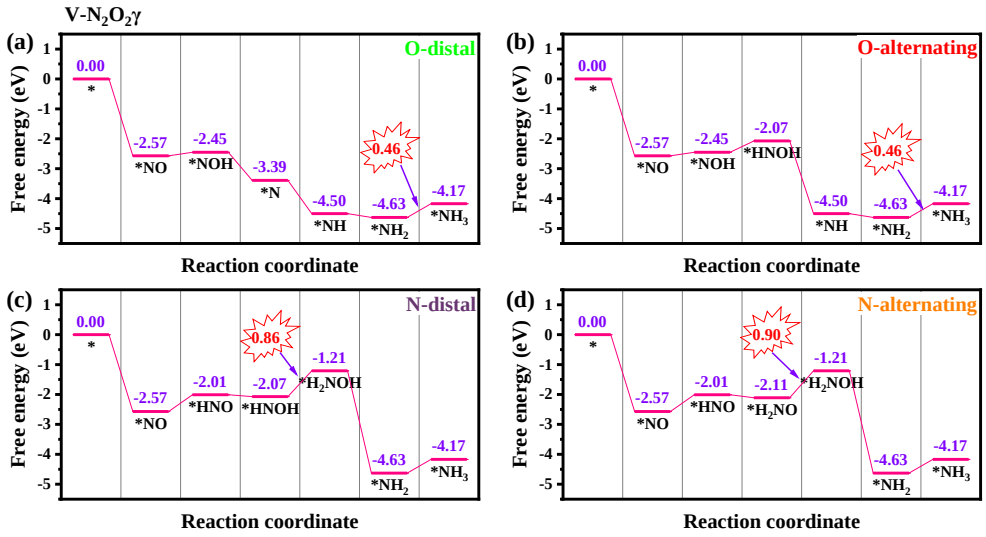

Fig. S13 Free energy diagrams of NORR on V-$N_2O_2\gamma$ SAC.

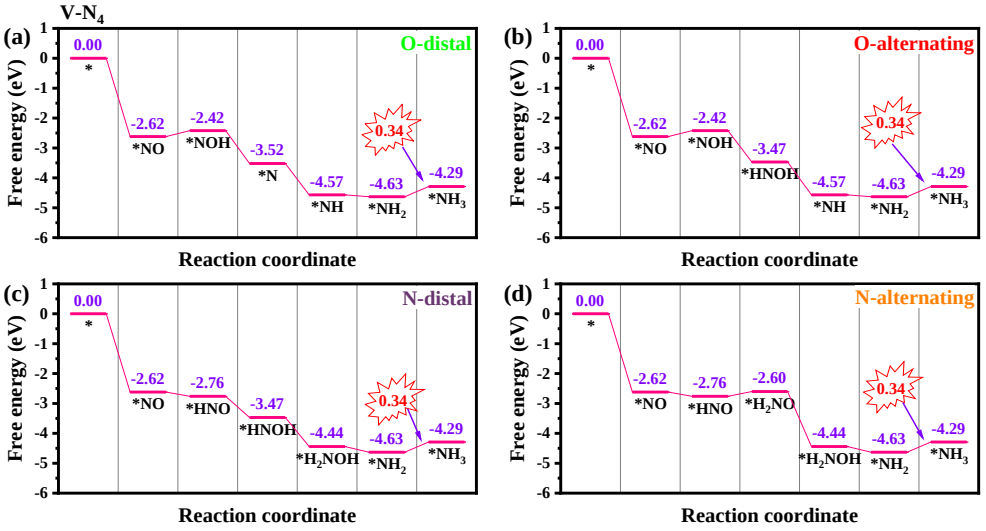

Fig. S14 Free energy diagrams of NORR on V-N_4 SAC.

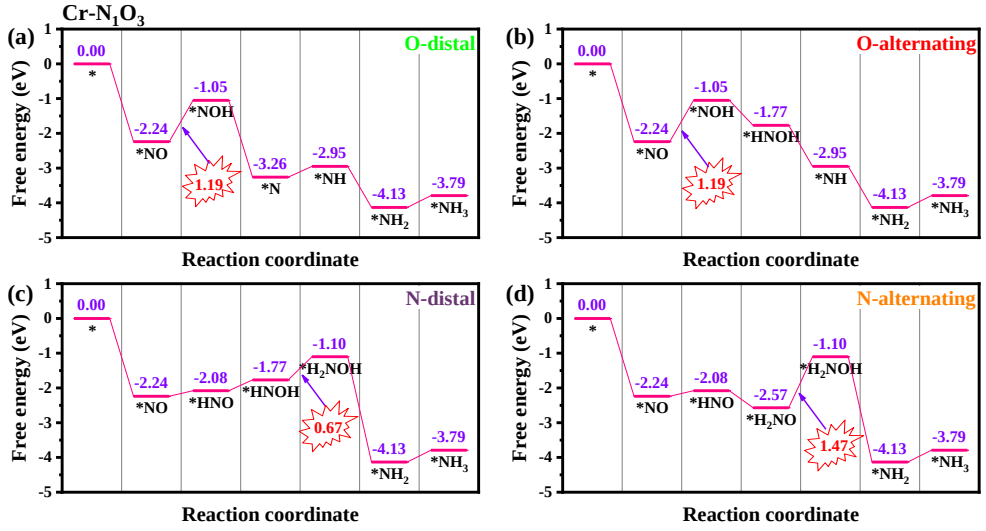

Fig. S15 Free energy diagrams of NORR on Cr-N_1O_3 SAC.

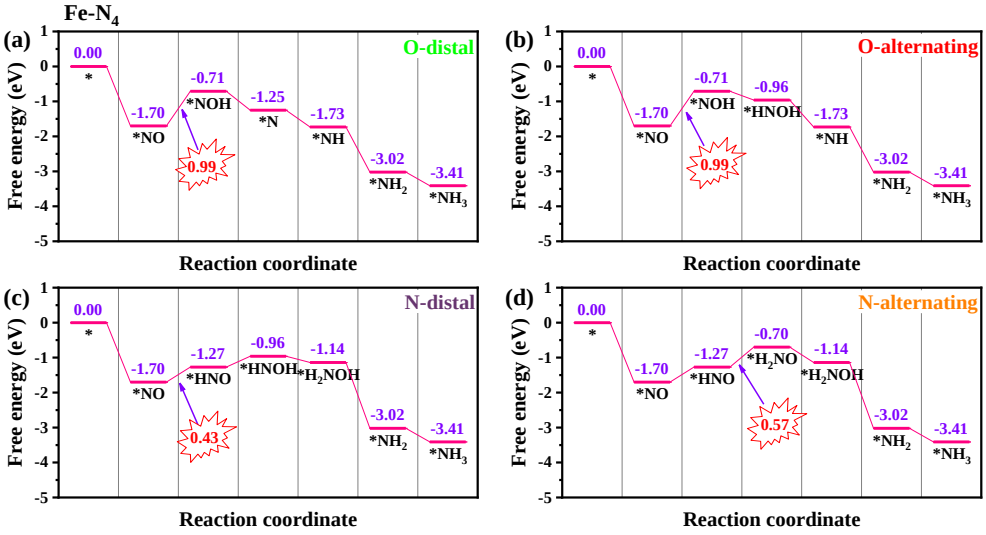

Fig. S16 Free energy diagrams of NORR on Fe-N_4 SAC.

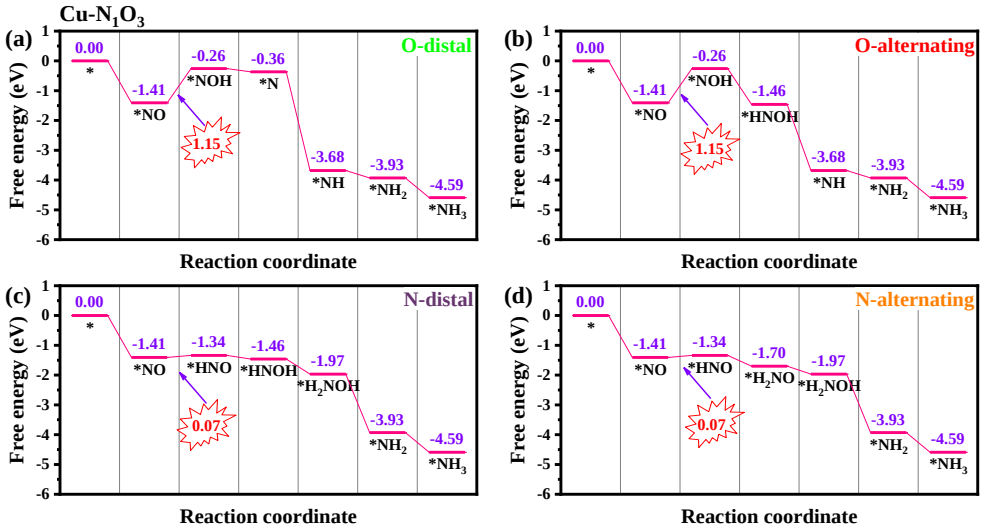

Fig. S17 Free energy diagrams of NORR on Cu-N_1O_3 SAC.

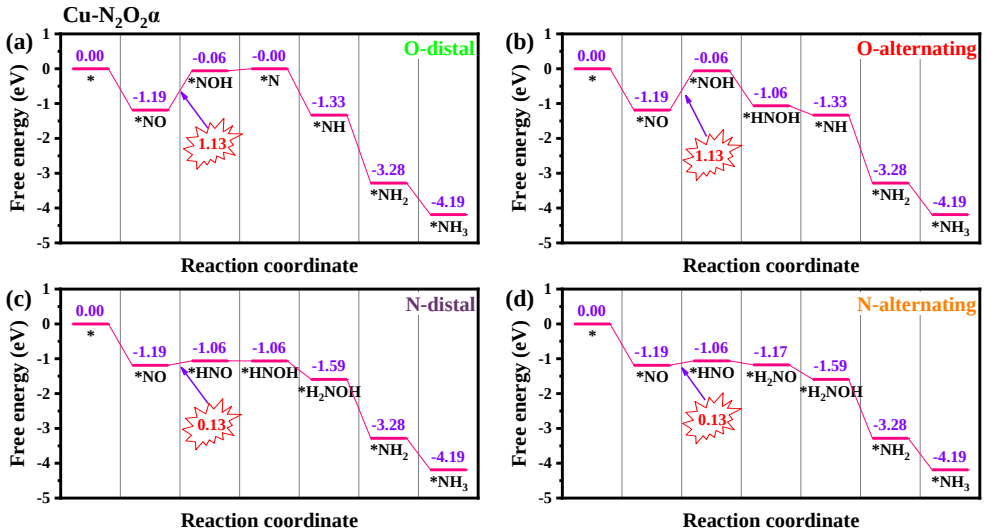

Fig. S18 Free energy diagrams of NORR on Cu-N_2O_2α SAC.

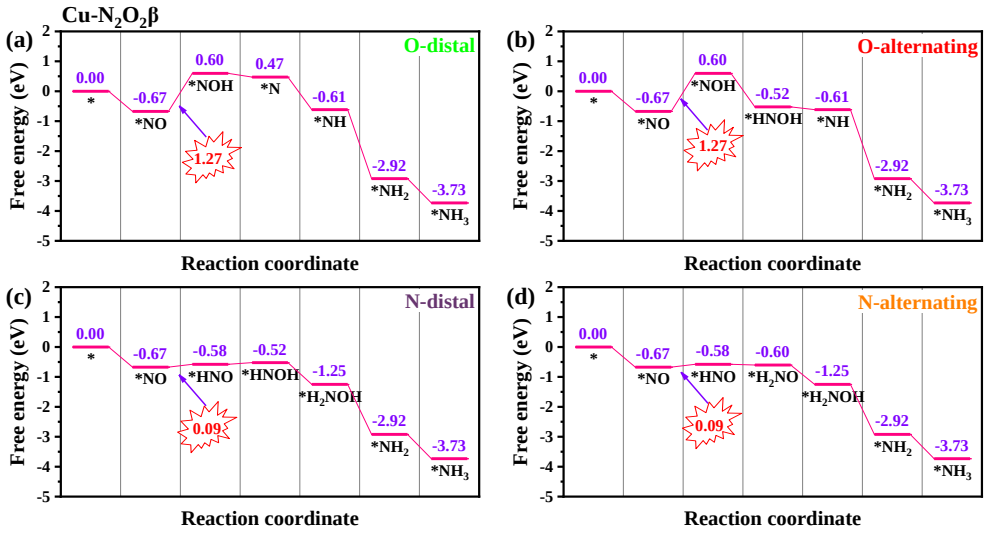

Fig. S19 Free energy diagrams of NORR on Cu-$N_2O_2\beta$ SAC.

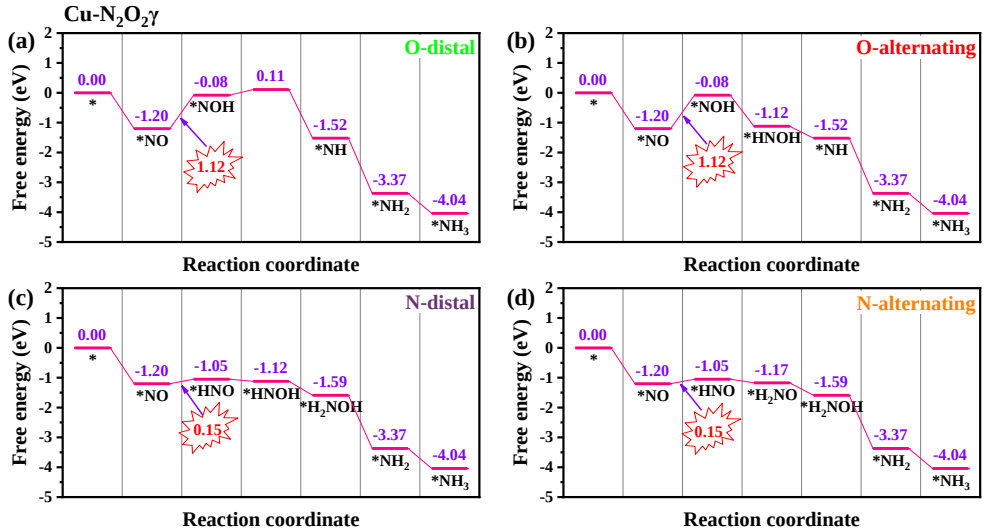

Fig. S20 Free energy diagrams of NORR on Cu-$N_2O_2\gamma$ SAC.

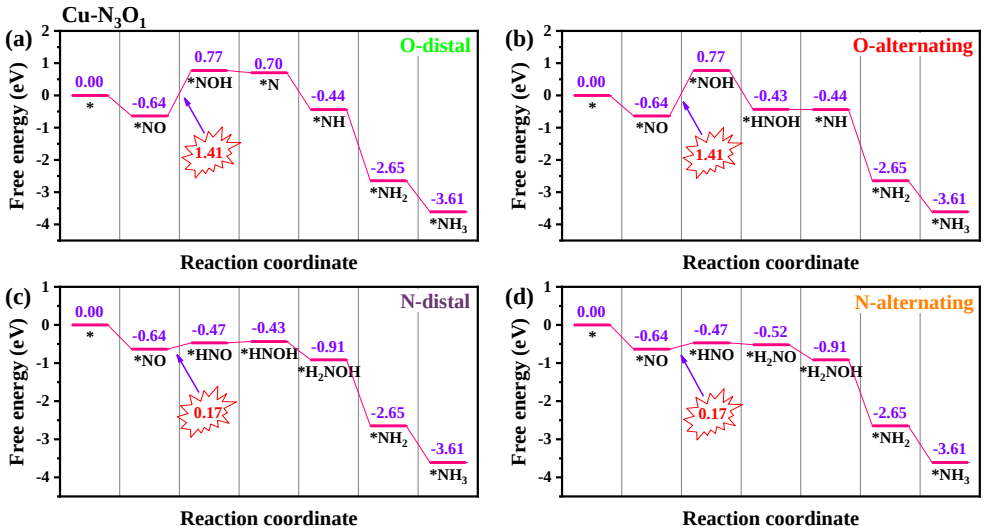

Fig. S21 Free energy diagrams of NORR on Cu-N_3O_1 SAC.

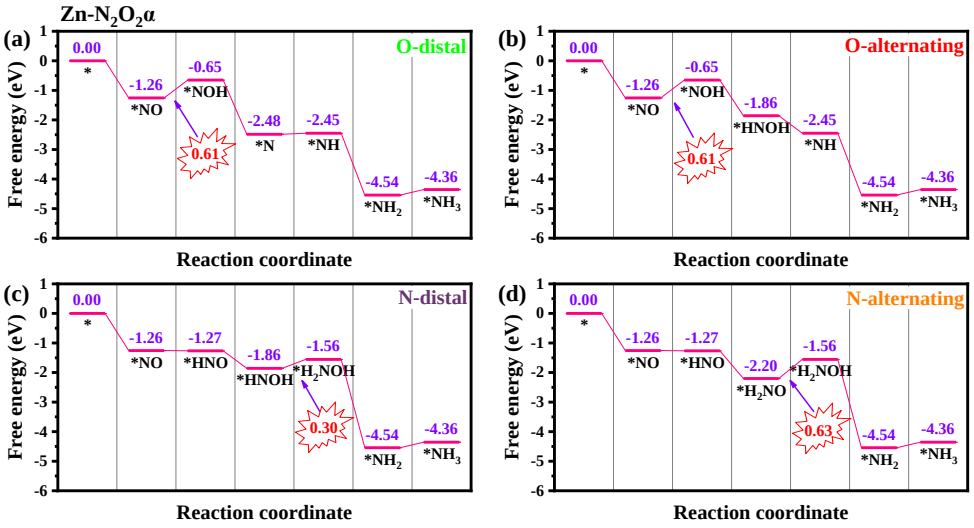

Fig. S22 Free energy diagrams of NORR on Zn-$N_2O_2\alpha$ SAC.

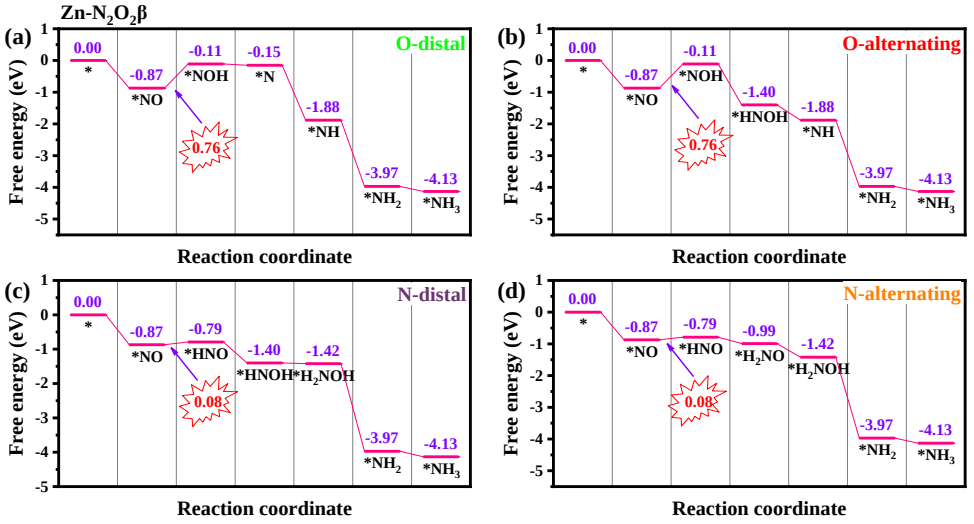

Fig. S23 Free energy diagrams of NORR on Zn-$N_2O_2\beta$ SAC.

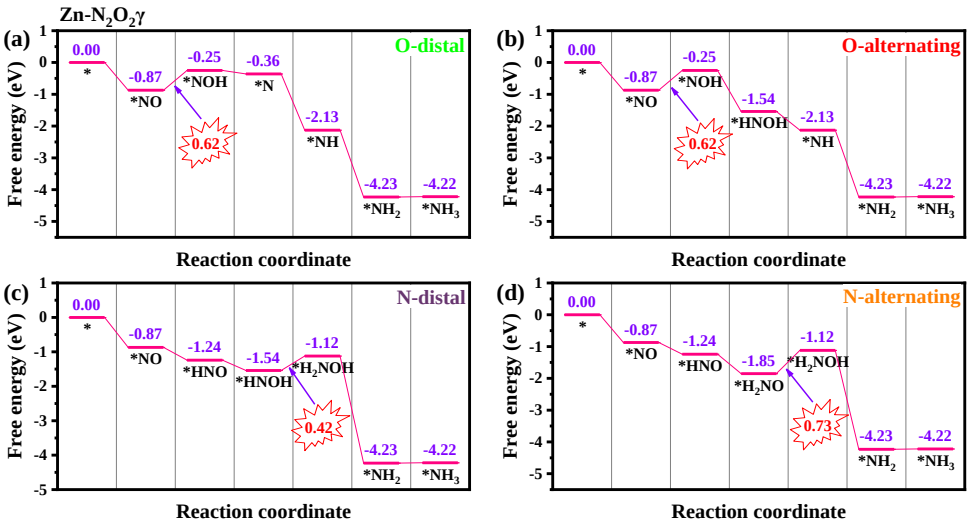

Fig. S24 Free energy diagrams of NORR on Zn-$N_2O_2\gamma$ SAC.

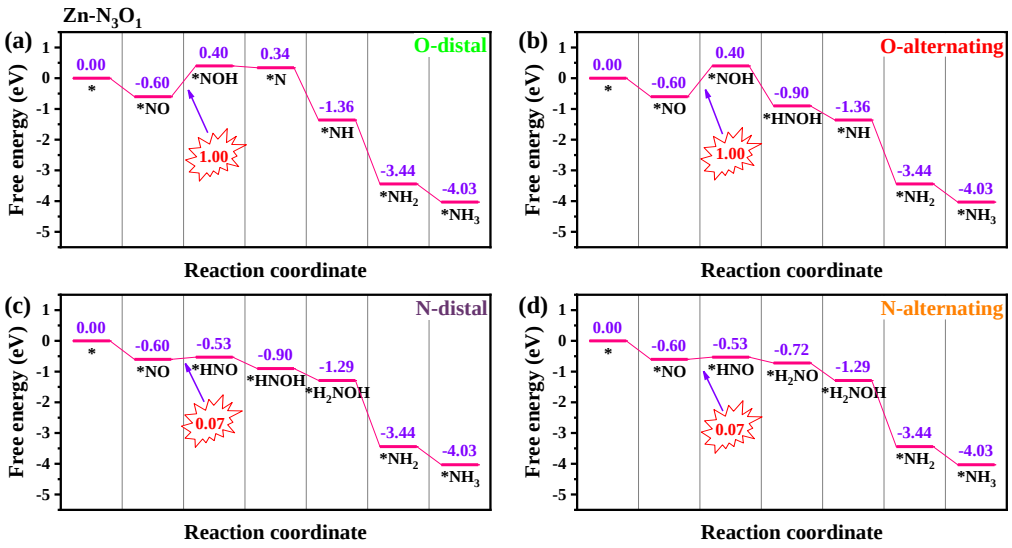

Fig. S25 Free energy diagrams of NORR on Zn-N_3O_1 SAC.

S14. Ab initio molecular dynamics simulation results

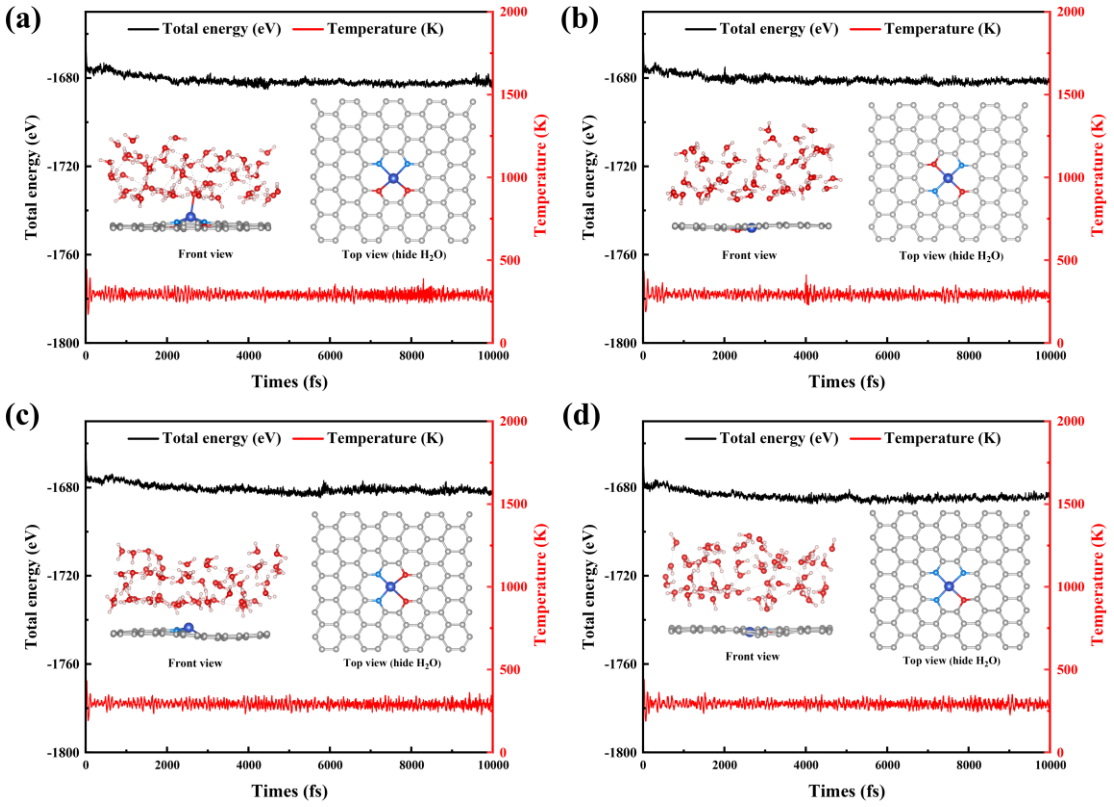

Fig. S26 Variations of total energy and temperature with simulation time for (a) Cu-$N_2O_2\alpha$, (b) Cu-$N_2O_2\beta$, (c) Cu-$N_2O_2\gamma$, and (d) Cu-N_3O_1 SACs. The insets show the front and top views of the structure after 10 ps simulations

S15. Machine learning results

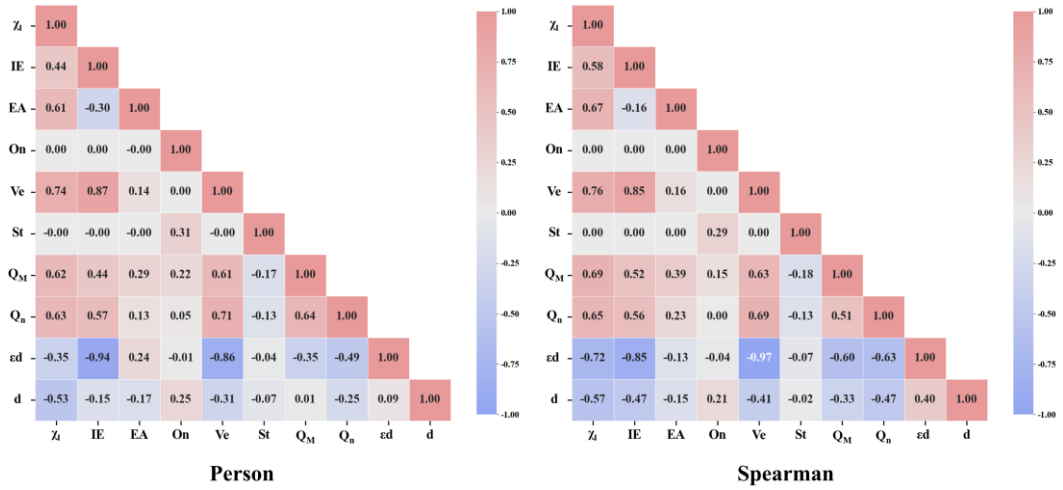

Fig. S27 Pearson and Spearman correlation heatmaps of 10 selected features .The two correlation methods show highly consistent overall trends

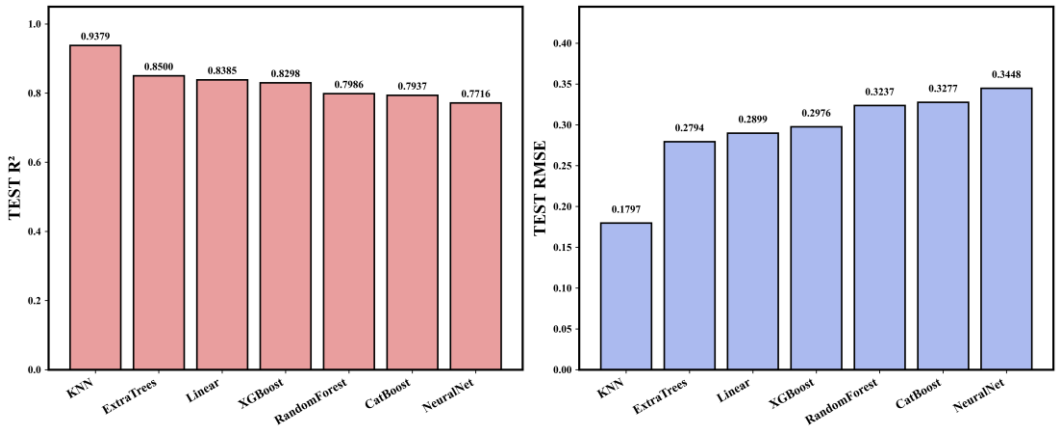

Fig. S28 Comparison of the predictive performance of seven ML models on the independent test set. The left panel shows the R^2 values and the right panel shows the RMSE values.

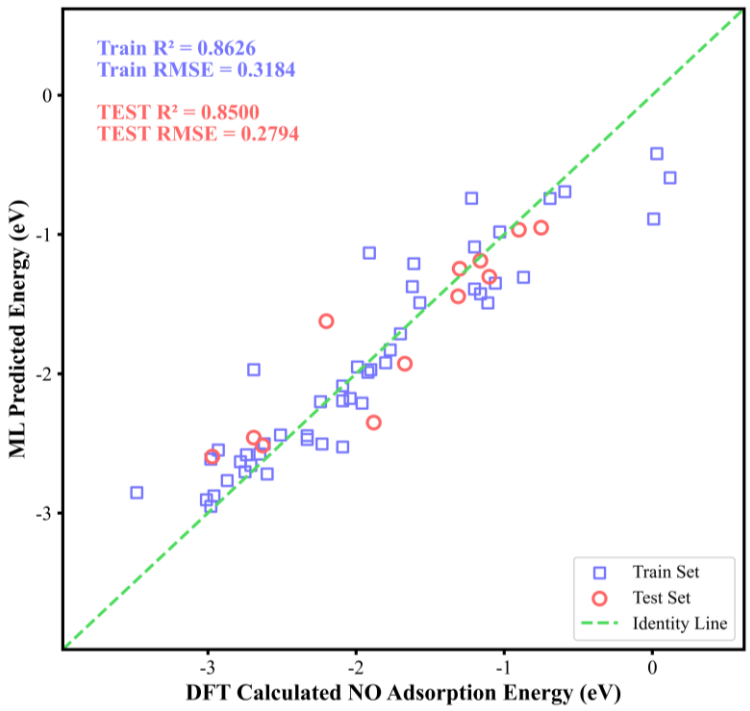

Fig. S29 ExtraTreesMSE model performance for predicting ΔG_{*NO}.

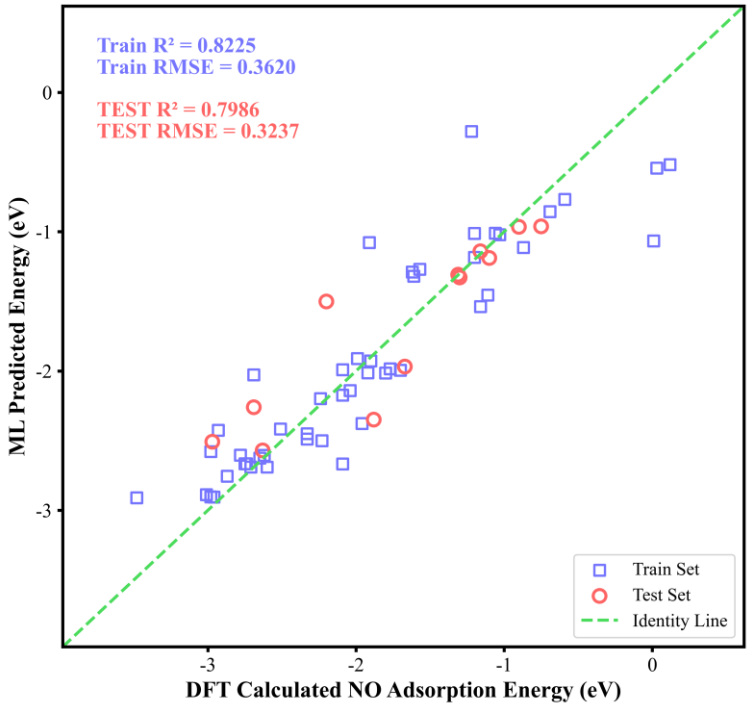

Fig. S30 RandomForestMSE model performance for predicting ΔG_{*NO}.

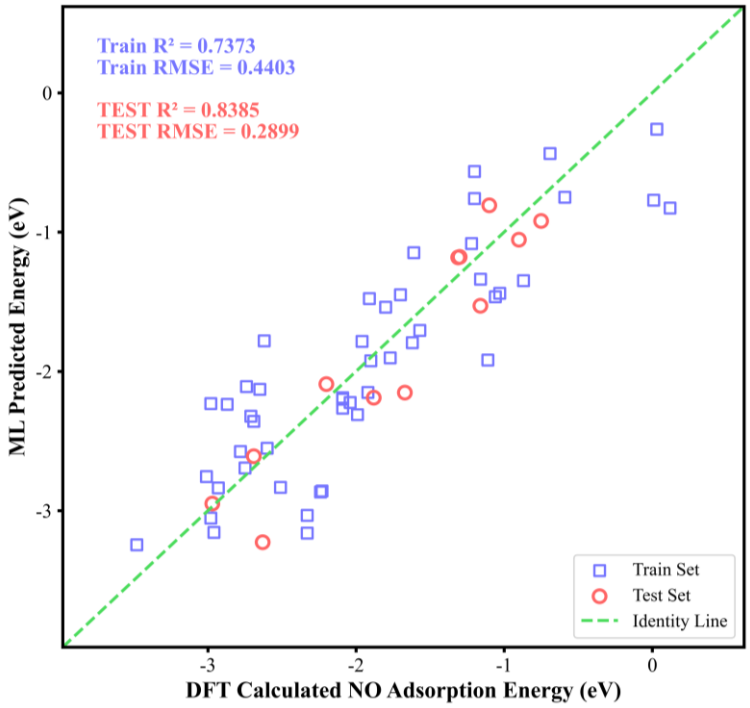

Fig. S31 Linear model performance for predicting ΔG_{*NO}.

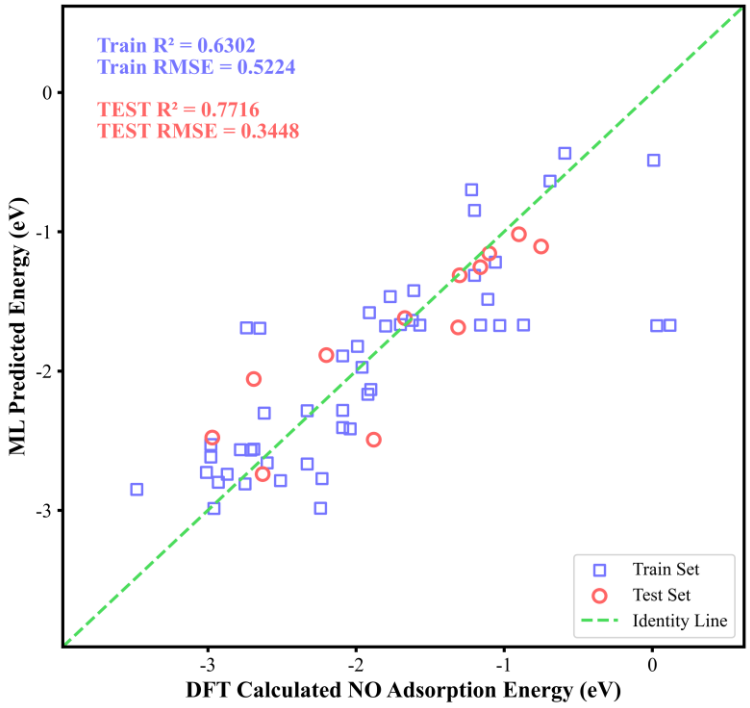

Fig. S32 NeuralNetTorch model performance for predicting ΔG_{*NO}.

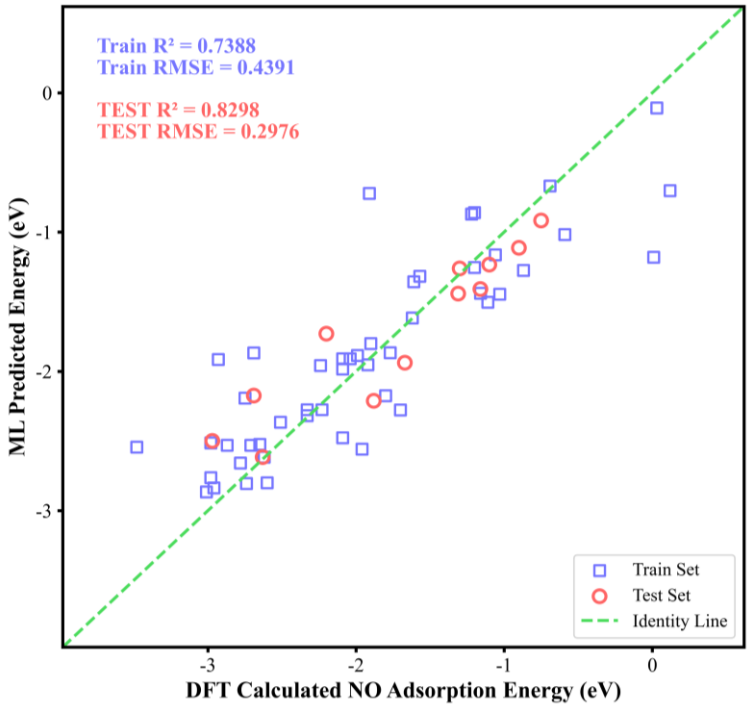

Fig. S33 XGBoost model performance for predicting ΔG_{*NO}.

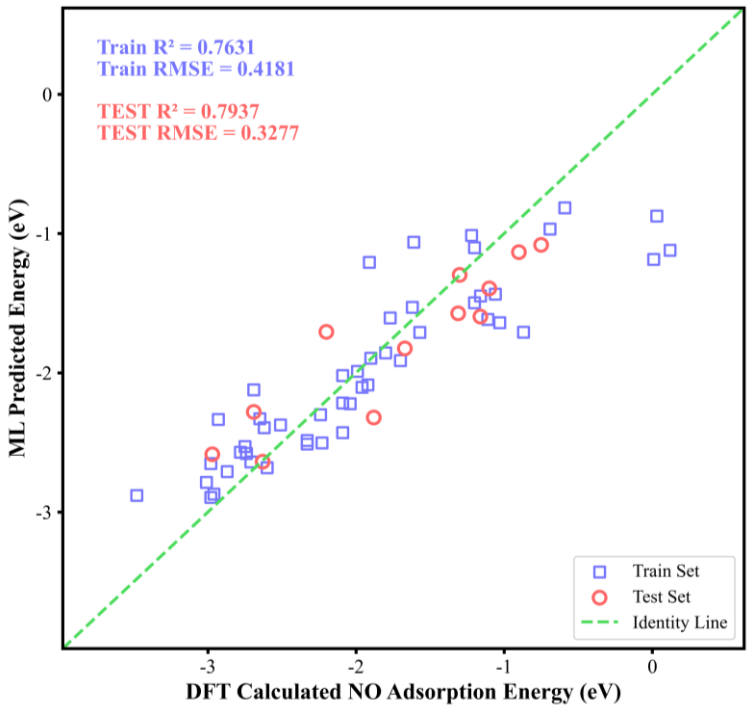

Fig. S34 CatBoost model performance for predicting ΔG_{*NO}.

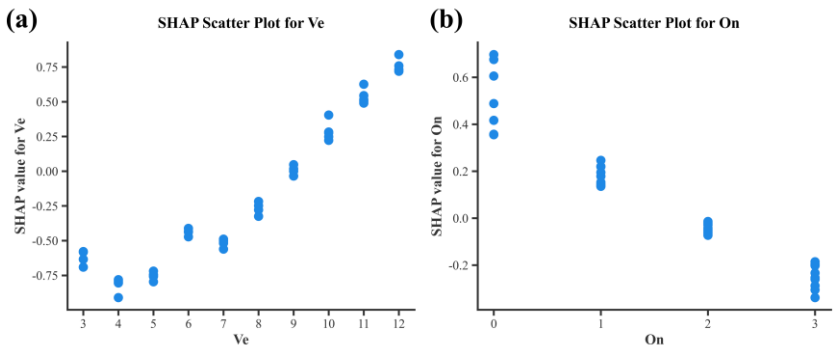

Fig. S35 SHAP-based interpretation of the ML model for ΔG_{*NO} prediction. (a) SHAP summary dot plot showing the global importance of all descriptors and the distribution of their impacts on the model output, and SHAP scatter plot for (b) Ve and On. In panels (b) and (c), the x-axis represents the descriptor value and the y-axis represents the corresponding SHAP value.

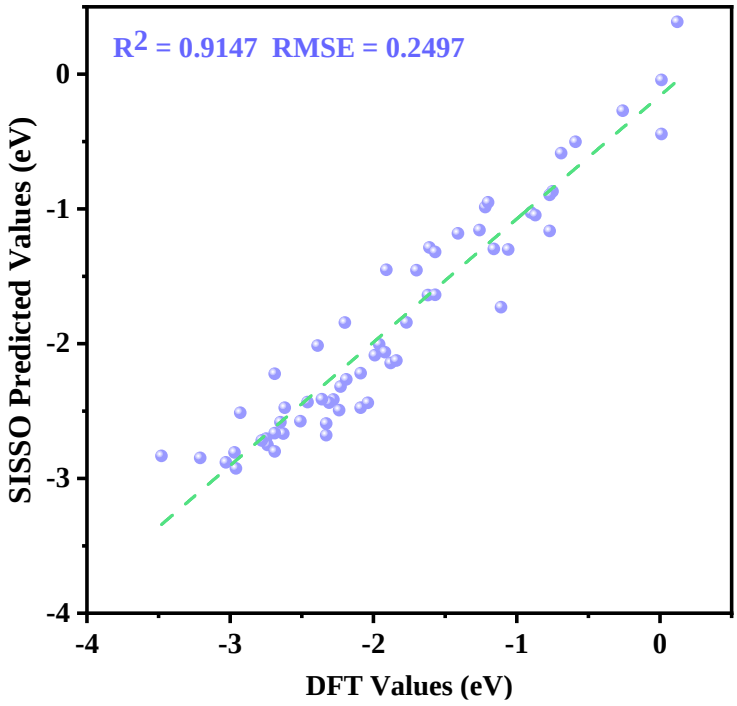

Fig. S36 SISSO predictions for ΔG_{*NO} compared to DFT-calculated values

To explore the potential applicability of the SISSO-derived descriptor beyond the training dataset, we performed additional calculations on a set of 10 previously unseen M-N_3O SACs containing 4d transition metals. For each system, the adsorption free energy of NO (ΔG_{*NO}) was computed using DFT and compared to the values predicted by the descriptor. The comparison in **Fig. S37** shows a moderate correlation between predicted and DFT-computed ΔG_{*NO} values, with $R^2 = 0.5992$ and RMSE = 0.5791 eV. While the descriptor qualitatively captures the overall trend of NO adsorption across these chemically related SACs, the quantitative accuracy is limited, reflecting the extrapolation beyond the chemical space of 3d M-N_xO_{4-x} SACs used for model training. These results indicate that the descriptor can provide trend-level insights for out-of-sample SACs, but additional first-principles validation is necessary when applying the SISSO-derived descriptor to systems with substantially different metal centers or coordination environments.

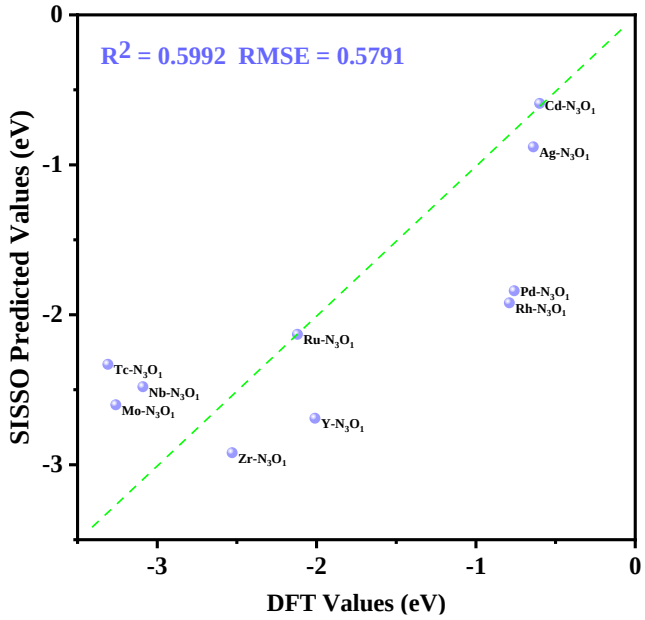

Fig. S37 Comparison of DFT-computed and SISSO-predicted ΔG_{*NO} values for a set of 10 previously unseen 4d-metal M-N_3O SACs.

References

[S1] Ma, Z.; Luo, Y.; Wu, P.; Zhong, J.; Ling, C.; Yu, Y.; Xia, X.; Song, B.; Ning, L.; Huang, Y. Unique Geometrical and Electronic Properties of TM_2-B_2 Quadruple Active Sites Supported on C_2N Monolayer Toward Effective Electrochemical Urea Production. *Adv. Funct. Mater.* **2023**, *33* (35), 2302475.

[S2] Liu, H.; Zhang, D.; Wang, Y.; Li, H. Reversible Hydrogen Electrode (RHE) Scale Dependent Surface Pourbaix Diagram at Different pH. *Langmuir* **2024**, *40* (14), 7632-7638.